Catalysis Letters (2023) 153:2149–2156
https://doi.org/10.1007/s10562-022-04126-9

The Effect of Nickel Salt on OMS-2 Nanorods in Oxygen Reduction Reaction

Xinyu Zhang[1,2] · Jun Zhang[2] · Yaya Sun[1] · Xiang Liu[1] · Dong-Sheng Li[1,3]

Received: 10 June 2022 / Accepted: 20 July 2022 / Published online: 27 August 2022

Abstract

The practical applications of Pt-based nano-catalysts in oxygen reduction reaction (ORR) have been seriously restricted by their high cost and poor durability. Therefore, it is significantly desirable to explore high active, non-noble metal and low-cost electrocatalysts for ORR. Herein, a series of nickel salts [$NiNH_2SO_3$, $Ni(NO_3)_2$, $NiSO_4$, $NiAc_2$, $NiCl_2$, and $Ni(acac)_2$] doped MnO_2 octahedral molecular sieves (Ni-OMS-2) nanomaterials are successfully synthesized by a simple hydrothermal reaction and used as cathodic ORR electrocatalyst. We also demonstrate that nickel salt has a significant influence on the porous structure, morphology and ORR performance. Notably, comparing with other nickel salts-doped Ni-OMS-2 catalysts, the resulting Ni-OMS-2 with $NiNH_2SO_3$ dopant exhibits impressive electrocatalytic performance toward ORR in alkaline (0.1 M KOH), with a more positive E_{onset} (0.866 V) and $E_{1/2}$ (0.792 V), as well as high limited diffusion current (5.03 mA/cm^2), respectively. Moreover, it displays superior long-term stability and methanol tolerance than that of commercial Pt/C, and the ORR process follows an ideal 4e$^-$ transfer pathway. Such outstanding ORR performance primarily contributes to the well-defined one-dimensional nanorods and nickel salts doping, which are in favor of promoting electron transfer, active sites exposure and intermediates absorption during the catalytic process.

Graphical Abstract

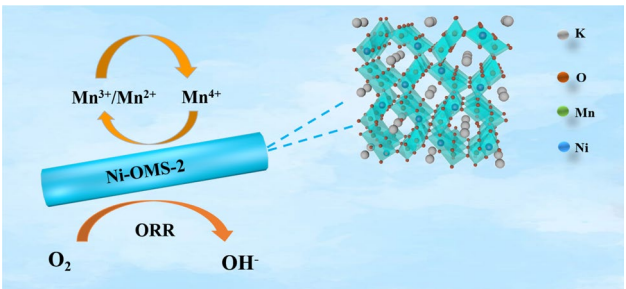

Keywords OMS-2 · Ni dopants · Electrocatalyst · ORR · Nanorod

✉ Jun Zhang
junzhang@cqust.edu.cn

✉ Xiang Liu
xiang.liu@ctgu.edu.cn

[1] Key Laboratory of Inorganic Nonmetallic Crystalline and Energy Conversion Materials, College of Materials and Chemical Engineering, China Three Gorges University, Yichang 443002, Hubei, China

[2] College of Metallurgy and Materials Engineering, Chongqing Key Laboratory of Nano/Micro Composites and Devices, Chongqing University of Science and Technology, Chongqing 401331, China

[3] Hubei Three Gorges Laboratory, Yichang 443002, Hubei, China

1 Introduction

As human being enters the twenty-first century, it is of significant theoretical importance and practical meaning to develop green and renewable energy storage technologies and conversion devices due to the increasing concerns about the global traditional energy shortage issue and a series of associated environmental contamination [1, 2]. Among them, metal-air batteries and fuel cells, as the common electric energy storage and conversion devices, have been widely deemed as the most potential portable and auxiliary power generators because of their merits of green, low cost, simple structure, wide operating temperature range, high specific energy and high energy conversion efficiency [3–6]. The electric energy storage and conversion at the fuel cells and metal-air batteries provides a very practical solution for the storage, distribution, transmission and supply of electricity [7–10]. However, the industrial applications of both fuel cells and metal-air batteries have been severely limited by the thermodynamically sluggish kinetics and high polarization of oxygen reduction reaction (ORR) on the cathode [11–15]. In general, the noble metal Pt or Pt-based cathode catalysts have been widely regarded as the most high-efficiency electrocatalysts for ORR [16], however the practical applications have been seriously restricted by their high cost, limited abundance and poor durability [17–19]. Therefore, it is significantly desirable to explore high active, non-noble metal and low-cost electrocatalysts for ORR. [20, 21] Currently, manganese oxides (MnO_x) have been attracted considerable attention in alkaline media toward ORR due to their low cost, abundance, environmental friendliness, and outstanding catalytic performance [22]. Numerous researches have revealed the ORR performance of MnO_x catalyst are strong dependence on the size, morphology, crystal structure and phase [23]. For example, the MnO_x catalyst with Mn^{3+}/Mn^{4+} redox couple in the octahedral sites and vacancy in solid phase usually possesses excellent electrocatalytic performance toward ORR [24]. On the one hand, the Mn^{3+}/Mn^{4+} species are regarded as electrochemical mediator for ORR. A larger amount of Mn^{3+} ions are beneficial to increase the Jahn–Teller lattice distortions and regulate the electronic structure, which coud result in an enhanced oxygen adsorption ability and elongated the O–O bond located in adsorbed oxygen [25]. On the other hand, introducing native oxygen defects could manipulate the interaction between oxygen species and catalyst surface, and could enhance O_2 absorption [26]. However, MnO_x as a semiconductor material, the lower electrical conductivity significantly hampered its widespread applications. Therefore, it is highly desired to design advanced strategy to improve the electrocatalytic activity of MnO_x catalyst.

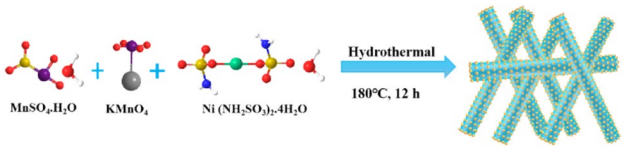

Scheme 1 The synthesis of Ni-OMS-2–1

To mitigate this drawback, a large number of strategies, such as conductive polymer or carbon introduction, morphology modification and cation doping, have been proposed to achieve outstanding ORR performance [27–32]. Currently, MnO_2 octahedral molecular sieves (OMS-2), with a 4.6×4.6 Å tubular structure, has received special attention in the fields of oxidation reaction, polluted water treatment and ORR [33–35], due to its highly porous structure, high abundance availability, high stability and coexistence of $Mn^{2+}/Mn^{3+}/Mn^{4+}$. [36–39] Especially, the unique OMS-2 material with well-defined one dimensional (1D) nanorod and tunable pore size are considerably conducive to improve the electrical conductivity and enhance the amount of surface active sites for ORR. Furthermore, research has also shown that incorporated cations (e.g., Co, Ni, Cu) appropriately into the lattice matrix of MnO_x are beneficial to achieve superior electrocatalytic performance [40, 41]. Miao group first reported the synthesis of Ni and Co-doped MnO_2 nanomaterials for the efficient ORR, with $E_{1/2}$ at 0.780 V [42]. In 2020, Yang group first reported the synthesis of OMS-2 nanorods filled with different concentrations of Co ions toward ORR via a simple hydrothermal reaction and exhibit outstanding ORR activity. The excellent ORR performance is the result of the following reasons: (i) incorporating cations into tunnel structure tailored the electronic structures and interconversion of Mn^{4+}/Mn^{3+} redox pair improved the inherent conductivity [43], (ii) as a regulatory substance, cations could effectively manipulated the coordination geometry and oxidation state of MnO_6 octahedron, for stabilizing Mn^{3+} by enhancing Mn–O covalency and increasing the O_2 adsorption ability for next conversion between oxygen and hydroxide [44]. Notably, enormous efforts have been devoted to designing cations doping and constructing OMS-2 nanomaterials for obtain efficient ORR performance, while rarely research has explored the influence of anion doping on the morphology, porous structure as well as ORR activity and durability of OMS-2.

Herein, we report a series of nickel salts doped MnO_2 octahedral molecular sieves Ni-OMS-2 **1–6** nanomaterials by a hydrothermal reaction of $KMnO_4$, $MnSO_4$ and various nickel salts (including nickel sulfaminate, nickel nitrate, nickel sulfate, nickel acetate, nickel chloride, and nickel acetylacetonate) for cathodic oxygen reduction reaction

under alkaline condition for the first time (Scheme 1). The effect of nickel salts on the crystal and porous structure, morphology and ORR performance have systematically investigated in this study. Then the optional Ni-OMS-2–**1** nanocomposite, which was doped with nickel sulfamate, exhibits the highest catalytic activity in ORR, with an onset and $E_{1/2}$ at 0.866 V *resp.* 0.792 V *vs.* RHE. Meanwhile, the resulting Ni-OMS-2–**1** catalyst shows outstanding stability and methanol tolerance relative to commercial Pt/C. These measurements are required for exploring the effect of nickel salts on OMS-2 nanorods in ORR.

2 Experimental

The synthesis of Ni-OMS-2–**1**: In briefly, Ni-OMS-2–**1** was prepared by following these steps: Potassium permanganate (1.8 mmol), manganese sulfate (0.6 mmol), and nickel sulfamate (0.8 mmol) were dissolved in 15 mL deionized water. After Stirring for 30 min, then transferred to a polytetrafluoron-lined reactor, which reacted at 180 ℃ for 12 h. Finally, the resulting precipitation was centrifuged and washed with deionized water for three times to obtain Ni-OMS-2–**1**. Other Ni-OMS-2 were synthesized under the same condition.

3 Results and Discussion

As shown in Scheme 1, a series of Ni-OMS-2 nanocomposites have been designed and prepared by a hydrothermal method from $KMnO_4$, $MnSO_4$ and various Ni salts with different anion [including $Ni(NH_2SO_3)_2$, $Ni(NO_3)_2$, $NiSO_4$, $Ni(Ac)_2$, $NiCl_2$, and $Ni(acac)_2$]. The final products are denoted as Ni-OMS-2 **1–6** corresponding to the Ni salt (Table 1). Then these Ni-OMS-2 **1–6** have been characterized by the powder X-ray diffraction (XRD), which were obtained from θ at 5° to 80° at 40 kV and 44 mA. As displayed in Fig. 1a, the crystal phase of only Ni-OMS-2**–1** prepared by this hydrothermal method is attributed to OMS-2 (JCPDS 44–0141) [45]. Ni-OMS-2 **2** and **3** retained most of the crystal phase of OMS-2, but a small part of crystal phase had been damaged by the doping of $Ni(NO_3)_2$ and $NiSO_4$, while a majority of OMS-2 phase of Ni-OMS-2 **4** and **5** had been destroyed by the doping of $Ni(Ac)_2$ and $NiCl_2$. Surprisingly, OMS-2 crystal phase of Ni-OMS-2–**6** had been totally destroyed by the doping of $Ni(acac)_2$, due to the super strong coordination ability of acetyl acetone with $Mn^{2+,3+}$ ions. As shown in Fig. 1b and c, these Ni-OMS-2 **1–6** nanocomposites have also been measured by the N_2 sorption isotherm to determine their BET surface areas, pore sizes and pore volumes, as summarized in Table 1. Except for Ni-OMS-2–**2** (23.6 m^2/g), their BET surface area has

Table 1 The surface area, pore volume, pore size, E_{onset}, $E_{1/2}$ and limiting current density of Ni-OMS-2 **1–6**

Examples	Ni salts	Surface area (m^2/g)	Pore volume (cm^3/g)	Pore size (nm)	E_{onset} (V)	$E_{1/2}$ (V)	J_L (mA/cm^2)
Ni-OMS-2–1	$Ni(NH_2SO_3)_2$	43.8	0.38	34.5	0.866	0.792	5.03
Ni-OMS-2–2	$Ni(NO_3)_2$	23.6	0.44	75.3	0.848	0.764	5.66
Ni-OMS-2–3	$NiSO_4$	47.9	0.36	29.8	0.856	0.755	5.21
Ni-OMS-2–4	$Ni(Ac)_2$	49.0	0.26	20.8	0.836	0.73	5.31
Ni-OMS-2–5	$NiCl_2$	48.7	0.35	28.4	0.842	0.725	5.32
Ni-OMS-2–6	$Ni(acac)_2$	32.4	0.07	9.0	0.832	0.635	4.96

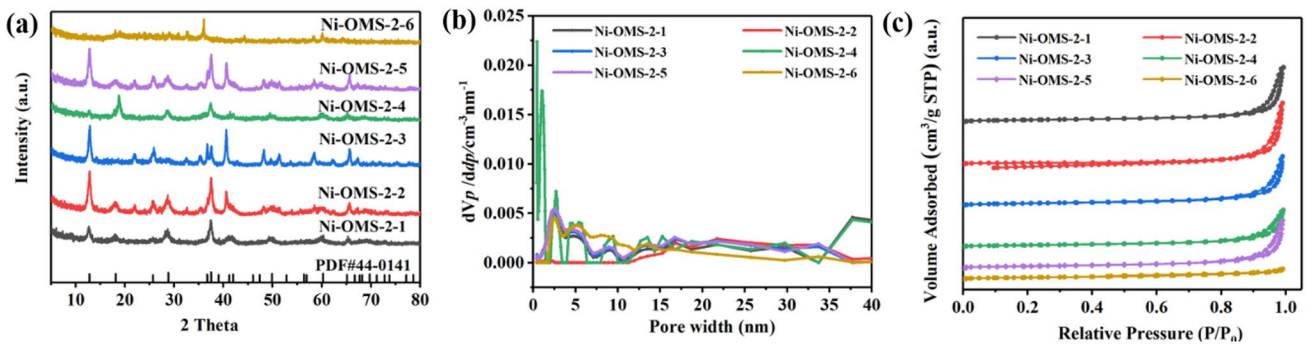

Fig. 1 **a** XRD, **b** BET and **c** pore diameter distribution of Ni-OMS-2 **1–6**

increased a lot in comparison to OMS-2 (26.45 m^2/g). The pore volume and size of Ni-OMS-2–**6** are only 0.07 cm^3/g and 9.0 nm, suggesting tunnel structure of OMS-2 had been totally destroyed. Moreover, the morphology and microstructure of these Ni-OMS-2 **1–6** nanocomposites have also been characterized by TEM. In Fig. 2, only Ni-OMS-2–**1** remains the well-defined nanorods-shaped morphology like pure OMS-2 nanorods (Fig. 2a). Unfortunately, as shown in Fig. 2b–e, the nanorods-shaped structure of Ni-OMS-2 **2–5** have been partially destroyed by doping Ni salts, especially that of Ni-OMS-2–**6** have been completely destroyed into nanoparticles (Fig. 2f), which are consistent with XRD results. The above results demonstrated that the Ni salts doping has an important influence on the morphology structure of Ni-OMS-2 catalysts, and the $NiNH_2SO_3$ is more conducive to construct 1D nanorods shapes, which favors the electronic transfer to obtain high ORR activity.

To investigate why Ni-OMS-2–**1** is so efficient in ORR, its SEM, HRTEM, energy dispersive X-ray spectrometry (EDX) and Raman spectrum have been further measured. Scanning electron microscope (SEM) images of Ni-OMS-2–**1** are further displayed in Fig. 3. It is clear that Ni-OMS-2–**1** possesses a nanorods-shaped structure, with a mean diameter and length of approximately 40 nm and 250 nm, respectively. Then, the lattice fringes of Ni-OMS-2–**1** have been provided from high-resolution TEM (HRTEM) images.

In Fig. 4, the crystal planes spaces of 0.220 nm, 0240 nm, 0304 nm and 0.488 nm are assigned to OMS-2 (420), (211), (340) *resp.* (200), suggesting Ni-OMS-2–**1** still remains the nanorods-shaped structure as pure OMS-2 [43]. For investigating the accurate localization of Ni in Ni-OMS-2–**1**, its EDX elemental mapping is also recorded in Fig. 5. Figure 5b shows that the homogeneous distributions of K (Fig. 5c), Mn (Fig. 5d), N (Fig. 5e), O (Fig. 5f), Ni (Fig. 5g) and S (Fig. 5h) throughout Ni-OMS-2–**1**. In Fig. 5g, the element of Ni is homogeneously dispersed onto the surface of OMS-2, suggesting that Ni atoms have been successfully doped into OMS-2. As illustrated in the Raman spectrum of Ni-OMS-2–**1** (Fig. 6), the peaks of Mn–O bond of MnO_6 octahedral in OMS-2 are placed at 496.88 cm^{-1}, 572.09 cm^{-1} and 628.98 cm^{-1}, being consistent with pure OMS-2 [46].

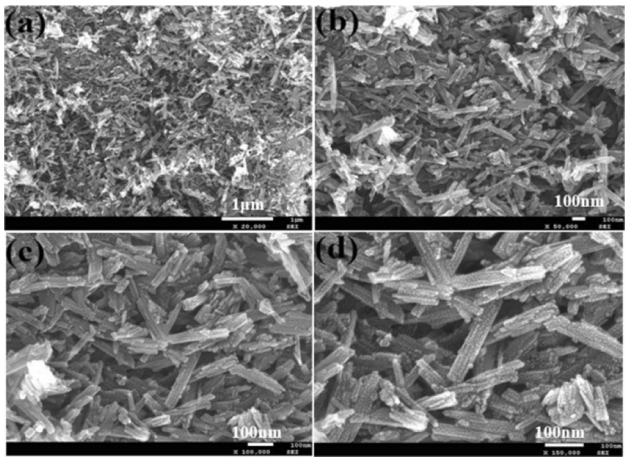

Fig. 3 SEM images of Ni-OMS-2–**1**

To investigation of the electrocatalytic ORR performance of different anion doping Ni-OMS-2 catalyst, the electrocatalytic properties of Ni-OMS-2 **1–6** have been evaluated by CV, LSV, stability test and methanol resistance test. As shown in Fig. S1, it can be seen a rectangular-like disappearance and then an obvious cathodic oxygen reduction peaks appearance when the electrolyte changes from N_2-saturated to O_2-saturated, which is evidenced all Ni-OMS-2 based catalysts has positive ORR performance [47]. Additionally, the $NiNH_2SO_3$ doped Ni-OMS-2 exhibits the most positive

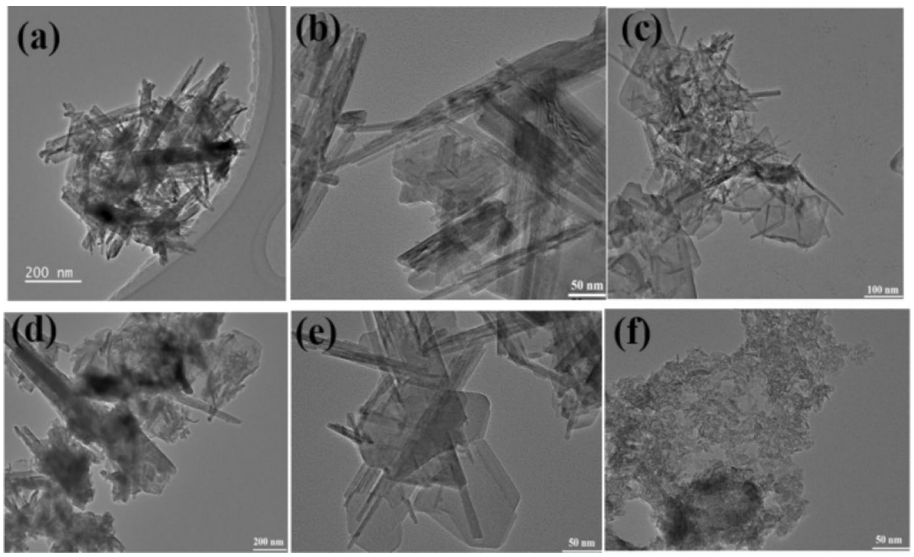

Fig. 2 TEM images of Ni-OMS-2 **1–6** nanocomposites

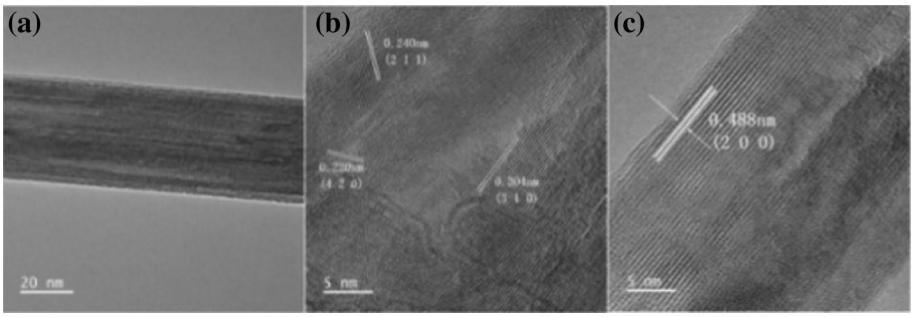

Fig. 4 **a**–**c** HRTEM images of Ni-OMS-2–**1**

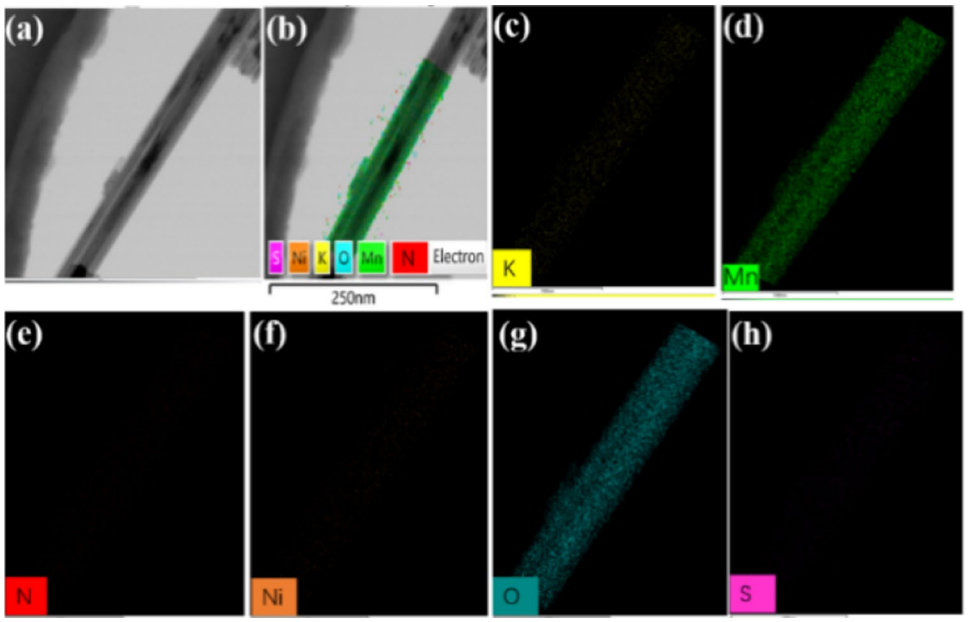

Fig. 5 **a** HAADF-STEM image, **b** Combined (S, Ni, K, O, Mn and N), **c** K, **d** Mn, **e** N, **f** O, **g** Ni and **h** S EDX compositional mapping of Ni-OMS-2–**1**

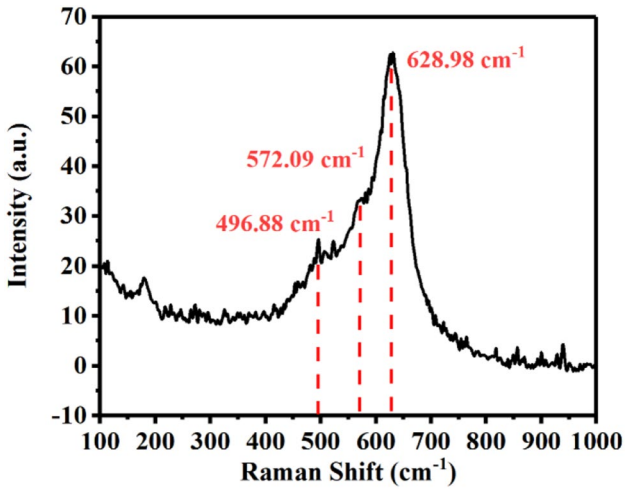

Fig. 6 Raman spectra of Ni-OMS-2–**1** nanocomposite

oxygen reduction peak potential compared with other anions doped Ni-OMS-2, indicating that Ni-OMS-2–**1** possesses more ORR activity (Fig. S1) [48]. The compared catalytic activities of these Ni-OMS-2 **1–6** nanocomposites for ORR in O_2 saturated 0.1 M KOH solution at 1600 rpm have been further measured in Fig. 7. All Ni-OMS-2 **1–6** nanocomposites exhibit the typical sigmoidal wave (Fig. 7a). As shown in Table 1, it is clear that Ni-OMS-2–**1** presents the highest catalytic activity toward ORR with E_{onset} of 0.866 V, $E_{1/2}$ of 0.792 V and J_L of 5.03 mA/cm^2 in a range of Ni-OMS-2 nanocomposites. The order of half-wave potential of Ni-OMS-2 **1–6** nanocomposites in ORR as follow: Ni-OMS-2–**1** (0.792 V) > Ni-OMS-2–**2** (0.764 V) > Ni-OMS-2–**3** (0.755 V) > Ni-OMS-2–**4** (0.73 V) > Ni-OMS-2–**5** (0.725 V) > Ni-OMS-2–**6** (0.635 V). This result is highlighting the dominant factor of Ni salts doping and nanorods-shaped structure in facilitating ORR in our system. To order to study the ORR pathway of Ni-OMS-2 **1–6** nanocomposites, LSV curves have also measured at various rotation rates from 800 to 2500 rpm (Figs. 7b and S2). It is obvious that dissolved O_2 is the first-order kinetic, based on the K–L plots [49]. The number of electron transfer for Ni-OMS-2–**1** is determined as 4.0 at a potential range of 0.3–0.5 V. Furthermore, Tafel slopes of Ni-OMS-2 **1–6** nanocomposites have been calculated in Fig. 7c, Ni-OMS-2–**1** exhibits an

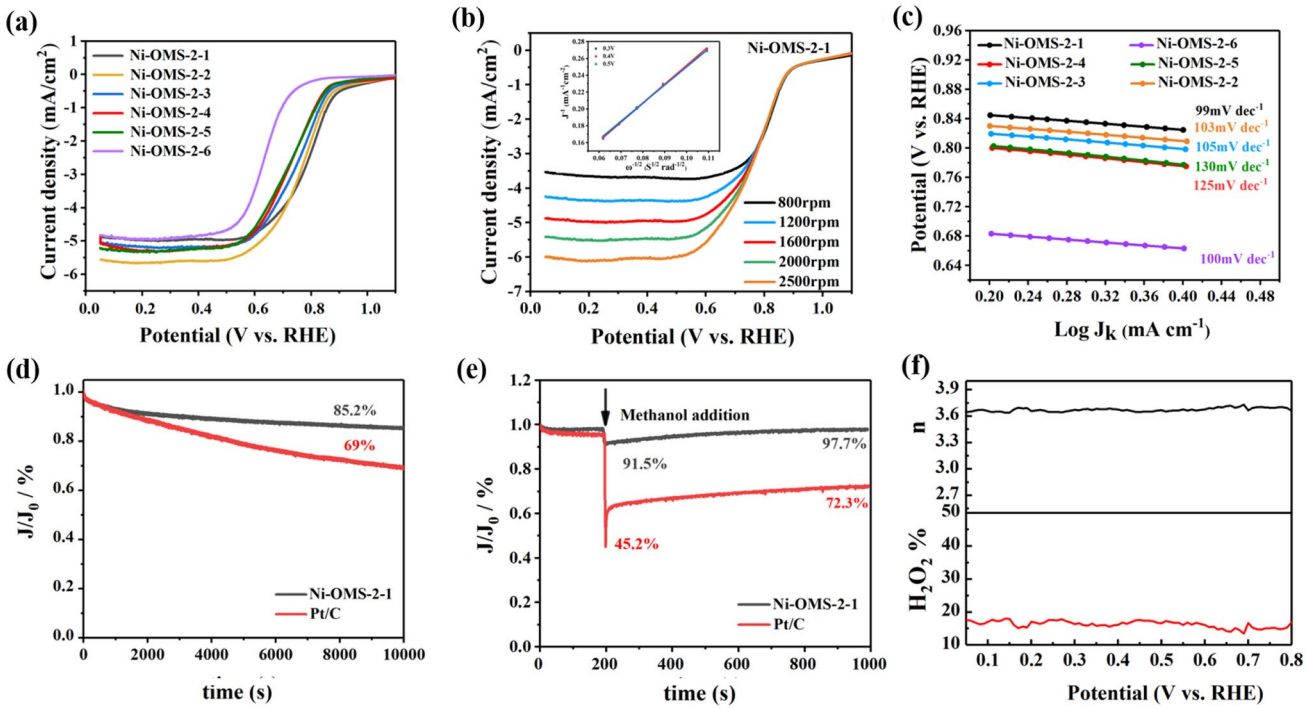

Fig. 7 **a** LSV curves of Ni-OMS-2–**1-6** recorded in O_2-saturated 0.1 M KOH solution at 1600 rpm; **b** LSV curves of Ni-OMS-2–**1** tested under various rotation speeds; **c** Tafel plots of Ni-OMS-2 **1–6** nanocomposites; **d** Chronoamperometric response of the commercial Pt/C and Ni-OMS-2–**1** at 0.5 V and **e** Chronoamperometric current density of the commercial Pt/C and Ni-OMS-2–**1** against operation time after adding CH_3OH. **f** H_2O_2 yield and electron transfer number vs. potential of Ni-OMS-2–**1**

Tafel slope of 99 mV/dec, which is lower than that of Ni-OMS-2–**2** (103 mV/dec), Ni-OMS-2–**3** (105 mV/dec), Ni-OMS-2–**4** (125 mV/dec), Ni-OMS-2–**5** (130 mV/dec) and Ni-OMS-2–**6** (100 mV/dec). According to the above analysis, the $NiNH_2SO_3$ doped Ni-OMS-2 catalyst demonstrates the most excellent ORR performance, which is may be ascribe to (i) the reserved MnO_6 octahedral in well-defined Ni-OMS-2–**1** nanorods could provide the excellent charge transfer performance [49], (ii) Ni-OMS-2–**1** also provides a good condition for stabilizing the Mn^{3+} active site, which is favor of ORR [50], (iii) the Ni atom introduced in Ni-OMS-2–**1** exhibit the superior interaction with OH^- species, which is contributing to the remarkable ORR activity [51, 52]. Therefore, the optimized Ni-OMS-2–**1** catalyst is used for further physical and electrochemical characterizations.

To further explore the stability and anti-methanol penetration, the stability of Ni-OMS-2–**1** has been further tested by the chronoamperometry process in Fig. 7d. The result reveals that the Ni-OMS-2–**1** still remains 85.2% current density after 10,000 s, which is remarkably higher than that of commercial Pt/C (69%). Meanwhile, the methanol resistance of Ni-OMS-2–**1** has also been studied under O_2-saturated KOH solution (0.1 M) in Fig. 7e. The current density of Pt/C catalyst reduces to 45.2% suddenly when the addition of 0.5 M CH_3OH solution, and then the current density will be returns to 72.3% until 1000 s. More interestingly, there is not obvious current density loss for Ni-OMS-2–**1** catalyst after the CH_3OH solution added, indicating that Ni-OMS-2–**1** exhibited the excellent methanol resistance for ORR [53]. As displayed in Fig. 7f, the calculated H_2O_2 yield and electron transfer number of Ni-OMS-2–**1** is 18% and 3.7, respectively, indicating the Ni-OMS-2–**1** catalyst follows a predominant four-electron transfer ORR pathway for the reduction of O_2 to OH^- [54].

To confirm surface chemical compositions and their valence states of Ni-OMS-2–**1**, its XPS has further been measured in Fig. 8. As shown in Fig. 8a, Ni, Mn, O, and K elemental signals have obviously recorded in the full XPS spectrum of Ni-OMS-2–**1**. As displayed in Fig. 8b, Mn 2p spectra of Ni-OMS-2–**1** with six peaks centered at 653.35 & 642.19 eV, 654.11 & 642.56 eV and 654.95 & 643.5 eV are corresponding to Mn^{2+}, Mn^{3+} and Mn^{4+}, respectively, the coexistence of $Mn^{2+}/Mn^{3+}/Mn^{4+}$ redox couple could facilitate transferring electrons from Mn^{3+} ion to O_2(ad) to obtain Mn^{4+}-$O_{2(ad)}$ [24, 55–58]. In Fig. 8c, Ni 2p spectra of Ni-OMS-2–**1** is deconvoluted into four peaks located at 872.66 & 849.81 eV and 874.12 & 855.27 eV, which are fitted to Ni (0) and Ni (II), respectively. Interestingly, as shown in Fig. 8d, O 1s spectra of Ni-OMS-2–**1** with two peaks placed at 531.88 eV and 530.09 eV are lattice oxygen

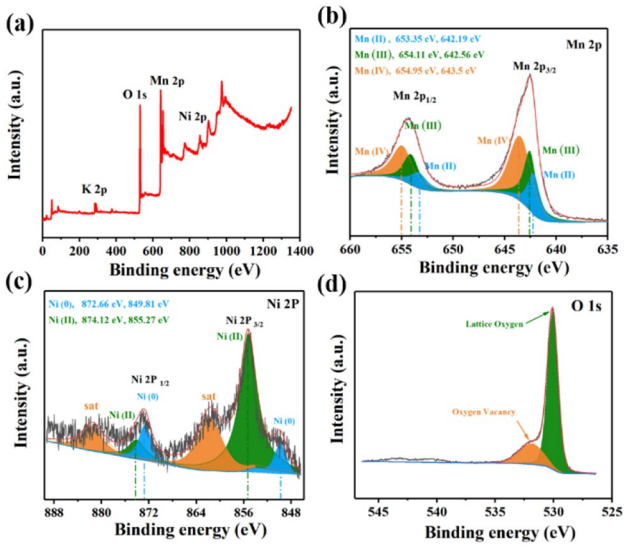

Fig. 8 XPS of **a** full spectrum, **b** Mn 2p, **c** Ni 2p and **d** O 1s in Ni-OMS-2–**1**

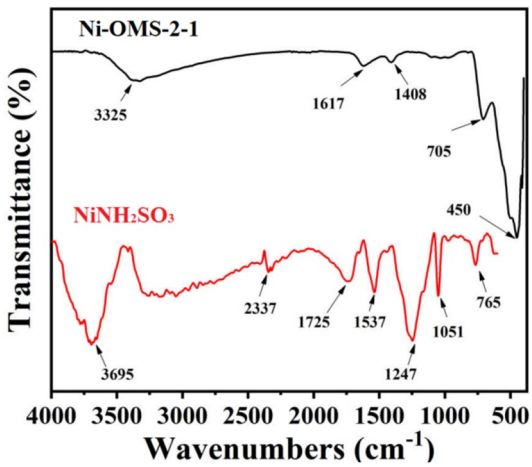

Fig. 9 FT-IR of Ni-OMS-2–**1** and $NiNH_2SO_3$

and oxygen vacancy, respectively, which is further increases the oxygen absorption.

In addition, Fourier Transform infrared spectroscopy (FT-IR) of Ni-OMS-2–**1** and $NiNH_2SO_3$ have been recorded in Fig. 9. It is clear that the characteristic peaks of $NH_2SO_3^{2-}$ did not appear in Ni-OMS-2–**1**, suggesting that only Ni^{2+} had been doped into OMS-2.

4 Conclusion

In summary, a series of nickel salts doped MnO_2 octahedral molecular sieves Ni-OMS-2 **1–6** nanomaterials, via a hydrothermal reaction of $KMnO_4$, $MnSO_4$ and various nickel salts (including nickel sulfaminate, nickel nitrate, nickel sulfate, nickel acetate, nickel chloride, and nickel acetylacetonate) have been developed for cathodic oxygen reduction reaction under alkaline condition for the first time. Detailed physical characterizations have verified that Ni-OMS-2–**1** exhibits a uniform nanorods-shaped structure with a mean diameter and length of approximately 40 nm and 250 nm, while the tunnel structure of other Ni-OMS-2 nanocomposites had been destroyed by the doping of Ni salts. Then the optional Ni-OMS-2–**1** nanocomposite, which was doped with $NiNH_2SO_3$, exhibits the highest catalytic activity in the ORR, with an E_{onset} and $E_{1/2}$ at 0.866 V *resp.* 0.792 V *vs.* RHE. Meanwhile, it displays a good electrochemical stability and methanol tolerance compared with Pt/C, and exhibits a predominant $4e^-$ transfer pathway. It seems that Ni embedded Ni-OMS-2–**1** not only provides a good condition for stabilizing the Mn^{3+} active site, but also exhibits the superior interaction with OH^- species, which is favor of ORR.

Supplementary Information The online version contains supplementary material available at https://doi.org/10.1007/s10562-022-04126-9.

Acknowledgements Financial support from the National Natural Science Foundation of China (No. 21805166), the 111 Project of China (No. D20015), the outstanding young and middle-aged science and technology innovation teams, Ministry of Education, Hubei province, China (T2020004), Foundation of Science and Technology Bureau of Yichang City (A21-3-012), the Science and Technology Research Program of Chongqing Municipal Education Commission (KJQN201901527), the Chongqing Research Program of Basic Research and Frontier Technology (cstc2019jcyj-msxmX0133), China Three Gorges University is gratefully acknowledged, thanks eceshi (www.eceshi.com) for the XPS analysis and Yuan Zhou from Shiyanjia Lab (www.shiyanjia.com) for HRTEM test.

Declarations

Conflict of interest The authors declare no competing financial interest.

References

1. Liu X, Zhang XY, Li DS, Zhang QC (2021) J Mater Chem A 9:18164–18174
2. Xu F, Liu X (2021) ACS Catal 11:13913–13920
3. Cheng W, Lu XF, Luan D, Lou XW (2020) Angew Chem Int Ed 59:18234–18239
4. Morales DM, Kazakova MA, Dieckhöfer S et al (2020) Adv Funct Mater 30:1905992
5. Chen D, Cao W, Liu J, Wang J, Li X, Jiang L (2021) J Energy Chem 59(2021):47–54
6. Yang X, Yi Q, Sheng K, Wang T (2020) Catal Lett 150:2886–2899
7. Gu Y, Min Y, Li L, Lian Y et al (2021) Chem Mater 33:4135–4145
8. Zhang T, Zhang S, Cao S, Ya Q, Lee JY (2018) Chem Mater 30:8270–8279
9. Xing X, Liu R, Cao K, Kaiser U et al (2018) ACS Appl Mater Interfaces 10:44511–44517

10. Fujimoto K, Ueda Y, Inohara D, Fujii Y et al (2020) Electrochim Acta 354:136592
11. Sun J, Du L, Sun B, Han G et al (2021) Energy Chem 54:217–224
12. Gu Y, Yan G, Lian Y, Qi P et al (2019) Energy Storage Mater 23:252–260
13. Zho Y, Xi S, Wang J, Sun S et al (2018) ACS Catal 8:673–677
14. Tian XL, Wang L, Chi B, Xu Y et al (2018) ACS Catal 8:8970–8975
15. Pan J, Xu YY, Yang H, Dong Z et al (2018) Adv Sci 5:1700691
16. Borghei M, Lehtonen J, Liu L, Rojas OJ (2018) Adv Mater 30:1703691
17. Wang HF, Chen L, Pang H, Kaskel S et al (2020) Chem Soc Rev 49:1414–1448
18. Ji Q, Bi L, Zhang J, Cao H, Zhao XS (2020) Energy Environ Sci 13:1408–1428
19. Tian X, Lu XF, Xia BY, Lou XW (2020) Joule 4:45–68
20. Hou CC, Zou L, Sun L, Zhang K et al (2020) Angew Chem Int Ed 59:7384–7389
21. Zhao CX, Li BQ, Liu JN, Zhang Q (2021) Angew Chem Int Ed 60:4448–4463
22. Cruz-Reyes I, Trujillo-Navarrete B, García-Tapia K, Salazar-Gastélum MI et al (2020) Fuel 279:118470
23. Lambert TN, Vigil JA, White SE, Delker CJ et al (2017) J Phys Chem C 121(5):2789–2797
24. Li Z, Yang Y, Relefors A, Kong X et al (2021) J Colloid Interface Sci 583:71–79
25. Li X, Ma X, Su D (2014) Nat Mater 13:586–592
26. Cheng F, Zhang T, Zhang Y (2013) Angew Chem Int Ed 52:2474–2477
27. Sun RM, Yao YQ, Wang AJ, Fang KM et al (2021) J Colloid Interface Sci 592:405–415
28. Lan B, Zheng X, Cheng G, Han J et al (2018) Electrochim Acta 283:459–466
29. Fang Y, Zhang T, Zhang Y, Zhu J (2021) Appl Catal A 627:118378
30. Zhang H, Wang Z, Ma C, Zhou Z, Cao L, Yang J (2020) ChemSusChem 13:6613–6620
31. Deng J, Lu H, Xu B, Cao Y, Yang W, Liu J (2021) Chem Eng J 413:127439
32. Chao G, Zhang Y, Zhang L, Zong W et al (2022) J Mater Chem A 10:5930–5936
33. Huang Y, Zheng K, Liu X, Meng X, Astruc D (2020) Inorg Chem Front 7:939–945
34. Bi X, Huang Y, Liu X, Yao N et al (2021) Technol 275:119141
35. He J, Wang M, Wang W, Miao R et al (2017) ACS Appl Mater Interfaces 9:42676–44268
36. Wang Y, Wang F, Fang Y, Zhu J et al (2019) Appl Surf Sci 496:143566
37. Hou W, Wang S, Bi X, Meng X, Zhao P, Liu X (2021) Chin Chem Lett 32:2513–2518
38. Cui C, Du G, Zhang K, An T et al (2020) J Alloys Compd 814:152239
39. Jiang M, Fu C, Yang J, Liu Q, Zhang J, Sun B (2019) Energy Storage Mater 18:34–42
40. Wang P, Lin Y, Wan L, Wang B (2019) ACS Appl Mater Interfaces 11:37701–37707
41. Choi Y, Lim D, Oh E, Lim C, Baeck SH (2019) J Mater Chem A 7:11659–11664
42. Chen B, Miao H, Yin M, Hu R et al (2021) Chem Eng J 417:129179
43. Hao Y, Li L, Lu Z, Yu X et al (2020) Appl Catal B 279:119373
44. Davis DJ, Lambert TN, Vigil JA (2014) J Phys Chem C 118:17342–17350
45. Huang Y, Liu J, Zhang J, Jin S et al (2019) RSC Adv 9:16313–16319
46. Gao T, Glerup M, Krumeich F, Nesper R et al (2008) J Phys Chem C 112:13134–13140
47. Yang L, Huang N, Luo C, Yu H et al (2021) Chem Eng J 404:127112
48. Wang T, He Y, Liu Y (2021) Nano Energy 79:105487
49. Selvakumar K, Duraisamy V, Venkateshwaran S et al (2022) ChemElectroChem 9:e202101303
50. Lee JM, Patil SB, Kang B, Lee S, Kim MG, Hwang SJ (2018) J Mater Chem A 6:12565–12573
51. Roche I, Chaînet E, Chatenet M, Vondrák J (2007) J Phys Chem C 111:1434–1443
52. Han Y, Yu Y, Zhang L, Huang L, Zhai J, Dong S (2018) Talanta 186:154–161
53. Zhan Z, Tan Y, Zeng T (2021) Nano Res 14:2353–2362
54. Shi C, Liu Y, Qi R (2021) Nano Energy 87:106153
55. Wang XT, Lin XF, Yu DS (2022) Rare Met 41:1160–1175
56. Xiong C, Wang T, Zhang Y et al (2020) Int J Hydrogen Energy 47:2389–2398
57. Xiong C, Li B, Liu H et al (2020) J Mater Chem A 8:10898–10908
58. Xiong C, Yang Q, Dang W et al (2020) J Power Sources 447:227387